



## Nonlinear carrier dynamics in silicon nano-waveguides

I. ALDAYA,<sup>1,†</sup> A. GIL-MOLINA,<sup>1,2,†</sup> J. L. PITA,<sup>2</sup> L. H. GABRIELLI,<sup>2</sup> H. L. FRAGNITO,<sup>1,3</sup> AND P. DAINESE<sup>1,\*</sup>

<sup>1</sup>Gleb Wataghin Physics Institute, University of Campinas, Campinas, SP, Brazil

<sup>2</sup>School of Electrical and Computer Engineering, University of Campinas, Campinas, SP, Brazil

<sup>3</sup>MackGrphe-Graphene and Nanomaterials Research Center, Mackenzie Presbyterian University, São Paulo, SP, Brazil

\*Corresponding author: [dainese@ifi.unicamp.br](mailto:dainese@ifi.unicamp.br)

Received 27 June 2017; revised 13 August 2017; accepted 1 September 2017 (Doc. ID 301117); published 5 October 2017

The understanding of free-carrier dynamics in silicon photonic nano-waveguides and micro-cavities is fundamental to several nonlinear optical phenomena. Through time-resolved pump and probe experiments, a complex and nonlinear carrier recombination dynamics is revealed. Our results show that the carrier lifetime varies as the recombination evolves, with faster decay rates at the initial stages (with lifetime of  $\sim 800$  ps) and much slower lifetimes at later stages (up to  $\sim 300$  ns). The large surface-to-volume ratio in nano-waveguides enables clear observation of the effect of carrier trapping, manifesting as a decay curve that is highly dependent on the initial carrier density. Further, we demonstrate faster recombination rates by operating at high carrier density. Our results, along with a theoretical framework based on trap-assisted recombination statistics applied to nano-waveguides, can impact the dynamics of several nonlinear nanophotonic devices in which free carriers play a critical role, and open further opportunities to enhance the performance of all-optical silicon-based devices. © 2017 Optical Society of America

**OCIS codes:** (130.3130) Integrated optics materials; (130.5990) Semiconductors; (250.4390) Nonlinear optics, integrated optics.

<https://doi.org/10.1364/OPTICA.4.001219>

### 1. INTRODUCTION

Free-carrier effects have a critical role in future silicon photonic circuits [1–4]. Fundamentally, both the dispersion and attenuation of optical modes in waveguides and cavities are modified in the presence of excess electron–hole pairs in the silicon core region, effects referred, respectively, as free-carrier dispersion (FCD) and free-carrier absorption (FCA) [5,6]. These two basic phenomena have been extensively explored in a variety of silicon-based photonic devices and applications. For example, carriers injected externally through a p-i-n structure in ring-resonators or in integrated Mach–Zehnder interferometers have been used to build fast optical modulators based on FCD-induced phase-shift [7,8]. Other devices based on FCA have also been demonstrated such as waveguide based optical attenuators with externally injected carriers [9].

Even in the absence of external injection, excess carriers can be generated optically due to silicon's relatively high two-photon absorption (TPA) coefficient at the 1550 nm telecommunication wavelength ( $\sim 0.7$  cm/GW) [10]. All-optical modulation has been achieved using TPA-generated free carriers using a high power control pump pulse [11]. Given silicon's high refractive index, in sub-micrometer structures the optical mode is tightly confined and nonlinear effects (such as TPA) appear at relatively low power. Several nonlinear phenomena and applications are therefore impacted by TPA-induced free carriers [2,3,12]. For example, free carriers impact the stability of soliton propagation

and self-breathing phenomena in silicon waveguides [4], give rise to FCD-induced soliton self-frequency shift, limit the efficiency of parametric and Raman amplification [2], improve the coherence while reducing the efficiency of supercontinuum generation [13], and limit the gain obtained in stimulated Brillouin scattering [14]. Analogously, there are also a number of nonlinear phenomena impacted by free carriers in micro-cavities [15,16].

FCD and FCA are not the only effects caused by excess carriers. Because silicon is a material with indirect bandgap, excess carriers recombine dominantly through a phonon-assisted process, which ultimately gives rise to an increase in the device temperature. This in turn modifies the refractive index through the thermo-optic effect. In this context, self-oscillation in micro-cavities is an interesting example [15–17]: first, the cavity resonance shifts due to FCD, and second, an opposite shift arises due to the temperature increase as a result of carrier recombination.

In the applications discussed above, any time domain analysis must take into account the dynamics of carrier generation, spatial diffusion, and recombination. Optical generation is generally assumed to be instantaneous, relative to the time scale in most photonic applications. Once a certain spatial distribution of carriers is created (e.g., following the square of the intensity profile in TPA generation), diffusion takes place. Obviously the rate at which carriers diffuse and the evolution of the spatial charge profile depends on the particular geometrical structure as well as on carrier mobility. For example, carrier diffusion has been extensively

modeled in photonic crystal cavities [18,19], as well as in rib-waveguide structures [20,21]. In those, carriers can diffuse out of the region in which the optical mode is confined. As a consequence, their impact on the optical mode (through FCD and FCA) ceases even before these carriers have recombined back to the valence band, simply because they have left the modal region. This is not necessarily the case in silicon strip waveguides, as the silicon core is completely surrounded by a dielectric material. The spatial distribution within the silicon core can evolve due to diffusion, but carriers no longer leave the modal region. In this case, recombination determines the rate at which free carriers cease to impact the optical mode.

In most photonic applications, carrier recombination is treated using an exponential time decay curve, generally characterized by a single lifetime. Although single-exponential decay is justified under certain conditions (i.e., minority-dominated carrier lifetime), generally speaking it is well known that recombination processes are strictly not single-exponential [22]. In silicon, band-to-band radiative recombination is generally neglected due to its indirect bandgap, and the main recombination mechanisms are (i) Auger recombination, which is significant only at high carrier densities (above  $10^{18} \text{ cm}^{-3}$ ) [23], and (ii) trap-assisted recombination, dominant in most cases [24,25]. In this paper, we explore the recombination of carriers in a silicon strip waveguide, under conditions that allow clear observation of complex recombination dynamics, particularly non-exponential decay. Using a pump and probe technique, we characterized the carrier dynamics for different excitation pulse powers and durations. Our results reveal faster decay rates at initial stages of recombination and slower ones at later stages. We experimentally observe the effect of trapping, leading to memory in the decay dynamics and we also demonstrate that operation at high carrier density leads to faster recombination rates. This paper is organized as follows: in Section 2 we describe our samples and our experimental methods; in Section 3 we present our results and discuss their implications to all-optical switching. In Section 4 we present a discussion of the results in terms of trap-assisted recombination, and we draw our conclusions in Section 5.

## 2. SAMPLES AND EXPERIMENTAL SETUP

We analyzed silicon on insulator waveguides with a cross section of  $450 \text{ nm} \times 220 \text{ nm}$  and length  $5.9 \text{ mm}$ . All samples had silicon dioxide cladding and were fabricated at the imec/Europractice facility (run no. 4048/14). A scanning electron microscope image of an unclad sample (before oxide deposition) can be seen in Fig. 1. Light was coupled in and out of the waveguides using

grating couplers. Coupling and propagation losses were evaluated at  $3.1 \text{ dB}$  and  $1.4 \text{ dB/cm}$  through linear regression of the measurements of three samples with different lengths ( $2.4$ ,  $5.9$ , and  $30 \text{ mm}$ ) under low input power.

Figure 2(a) shows the pump and probe experimental setup employed to characterize the free-carrier dynamics in the waveguide under test. The pulsed pump was synthesized by externally modulating a continuous wave (CW) laser operating at  $1547 \text{ nm}$  (with  $20 \text{ mW}$  optical power) using a Mach-Zehnder electro-optical modulator (EOM). The EOM was driven by a train of pulses with  $500 \text{ kHz}$  repetition rate and pulse duration ranging from  $130 \text{ ps}$  to  $20 \text{ ns}$ . The EOM used has  $20 \text{ GHz}$  bandwidth and more than  $30 \text{ dB}$  extinction ratio. The pump signal was then amplified using an erbium-doped fiber amplifier (EDFA). Special care was taken to avoid generation of free carriers outside the pump pulse window. First, the EOM bias voltage was set for maximum peak pump power at the output of the EDFA, minimizing any remaining CW level on the pump. Second, the output of the EDFA was filtered using an optical bandpass filter (BPF) to reduce the out-of-band amplified spontaneous emission (ASE), and an acousto-optic modulator (AOM), operating as an optical gate, filtered out any remaining CW components outside the pulse window (either from the pump or ASE). The AOM was driven with a  $20 \text{ ns}$  gate pulse duration and has an extinction ratio larger than  $50 \text{ dB}$ . The pump power was controlled with a variable optical attenuator (VOA) and a  $1\%$  fraction was derived and monitored in a scope for stability and power control. It is worth noting that this configuration, where the EOM is followed by an EDFA and the injected power is controlled through a VOA, enables us to achieve high peak power and keep the EDFA operating conditions constant. This ensures that the pulse shape for the different pump power levels is preserved. The pump was then combined with the CW probe (operating at  $1549 \text{ nm}$ ) using a  $10\text{--}90$  optical coupler and then injected into the waveguide. The probe power was set to  $-12 \text{ dBm}$  in the waveguide. Figure 2(b) shows the spectrum measured at the input, before coupling into the waveguide. The ASE power spectral level is below  $-60 \text{ dBm}$  in a  $0.01 \text{ nm}$  resolution bandwidth. After the waveguide,  $10\%$  of the output signal was monitored in a scope, and  $90\%$  was filtered through two cascaded BPFs to remove the pump (with more than  $40$  and  $50 \text{ dB}$  of rejection ratios). Before detection, the probe was amplified using a low-noise pre-EDFA and then filtered with a BPF to remove out-of-band ASE (with more than  $50 \text{ dB}$  of rejection ratio). Figure 2(c) shows the spectra before and after BPF4 identified in Fig. 2(a). A wide-bandwidth oscilloscope was used to capture the signals. The input to Channel 1 (an optical input with

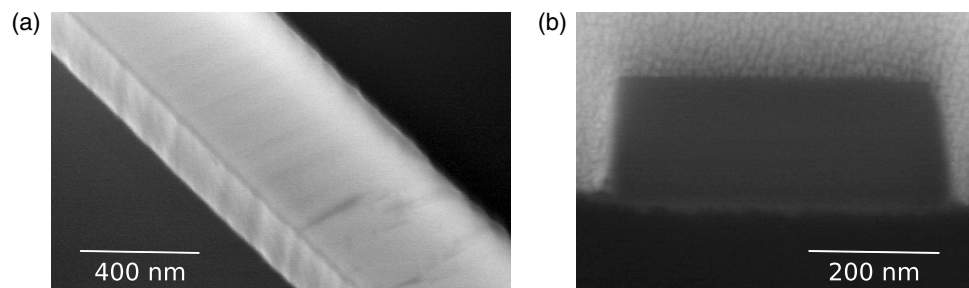


**Fig. 1.** Scanning electron microscope images for an unclad silicon strip waveguide of  $450 \text{ nm} \times 220 \text{ nm}$ , similar to the one used in our experiments: (a) perspective and (b) cross-section views.

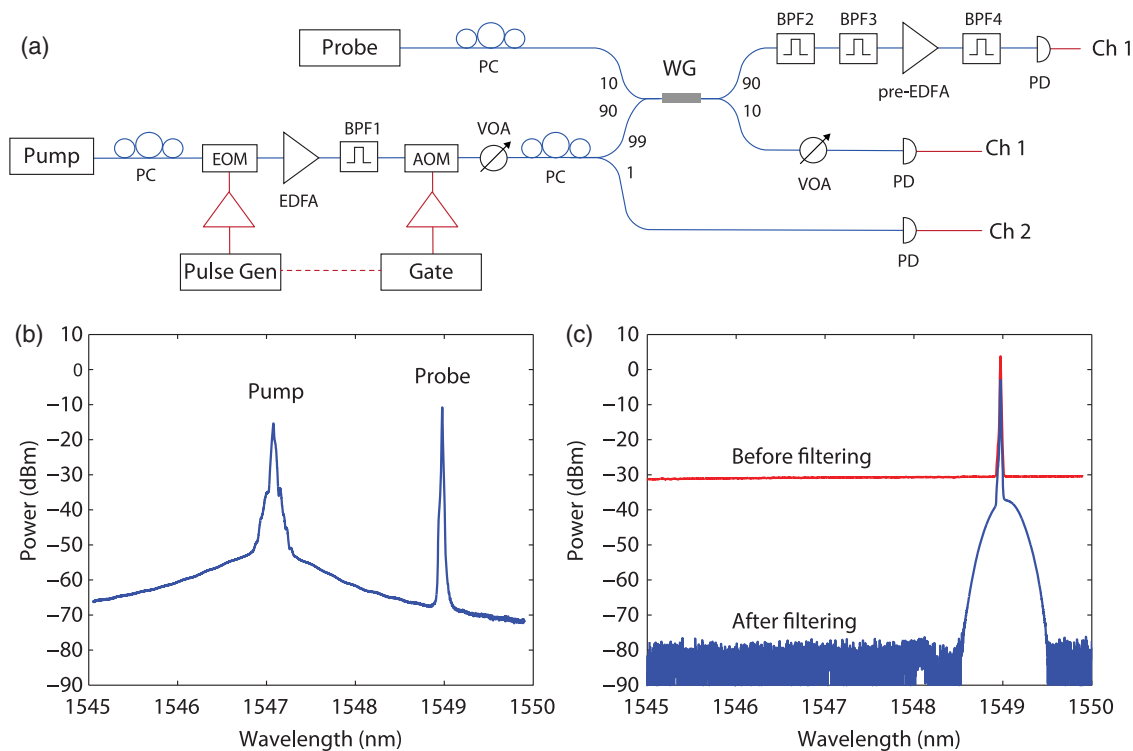


**Fig. 2.** (a) Experimental setup employed to characterize the free-carrier lifetime in SOI strip waveguides. WG, waveguide under test. Other acronyms are defined within the text. (b) Power spectrum at the input of WG. (c) Power spectra before and after BPF4.

a built-in 28 GHz photodetector, PD) was switched to measure either the filtered probe or the output pump pulses, whereas in Channel 2 (electrical input), the output of an external PD of 20 GHz bandwidth was captured to monitor the input pump pulses.

### 3. RESULTS

From the detected output probe signal, the nonlinear loss is obtained from the ratio between the detected signals for pump off and on (which therefore excludes linear losses). Since we are using wideband photodetectors to observe rapid lifetimes, several measurements were averaged to reduce high-frequency noise in the nonlinear loss curves (25 and 400 averages for the highest and lowest power, respectively). An example of the detected nonlinear loss is shown in Fig. 3(a) for a 130 ps pump pulse with 280 mW peak power in a waveguide of 5.9 mm. In the inset, two regimes can be identified: within the pump pulse duration, the nonlinear loss is dominated by instantaneous non-degenerate TPA, while after the pulse the nonlinear loss arises solely from FCA [26–28]. For waveguides with larger cross sections or structures that allow carriers to leave the modal region (e.g., photonic crystal cavities), an intermediate stage where diffusion plays a role has been reported [18,21,29]. However, as already mentioned, the nanowire structure investigated here confines the excess carriers to the core region, not allowing them to diffuse out. Moreover, for the small dimensions of the waveguide cross section explored in this paper, a non-uniform initial carrier distribution (just after the pulsed pump generation has ceased) diffuses throughout the entire core and becomes uniform in a relatively short period of time. In Supplement 1, an initial Gaussian distribution is shown to become uniform in approximately 5 ps for electrons and 15 ps

for holes, which is too short to be identified in Fig. 3(a). In the FCA-dominated regime, the nonlinear loss is determined by the accumulated FCA along the waveguide length:

$$L_{\text{FCA}}(t) = \exp \left[ \alpha_r \eta \int_0^L N(z, t) dz \right] = \exp[\alpha_r \eta \bar{N}(t)L], \quad (1)$$

where  $\eta$  accounts for the overlap between the free carriers in the silicon core and the optical mode profile. Given the fast diffusion of photo-generated carriers within the waveguide cross section [21], the traverse spatial distribution can be considered constant over the whole core, resulting in  $\eta = 0.77$ . Then,  $\alpha_r = 1.45 \times 10^{-17} \text{ cm}^2$  is the FCA cross section in silicon at 1550 nm [5,6],  $N(z, t)$  is the carrier density at a certain position  $z$  along the waveguide at an instant of time  $t$ , and  $L$  is the waveguide total length [30]. Here  $\bar{N}(t)$  is the average of the carrier density along the waveguide length. By inverting Eq. (1), we can extract the time-resolved carrier density average  $\bar{N}(t)$  from the measured nonlinear loss  $L_{\text{FCA}}$ . As shown in detail in Supplement 1, for the power levels and waveguide length explored in this paper,  $\bar{N}(t)$  approximates  $N(z, t)$  reasonably well. However, large deviations occur as pump power or waveguide length increase. From now on, we refer to  $\bar{N}(t)$  as simply carrier density (not specifying it is the averaged value).

Using the nonlinear loss from Fig. 3(a) in the FCA-dominated regime (i.e., for times after 4.2 ns), the obtained carrier density as a function of time is shown in Fig. 3(b) (blue curve). The result clearly shows that the free-carrier density does not decay following a simple exponential curve, as it is not a straight line in logarithmic scale. We repeated these measurements for pump power levels ranging from 0.07 to 1.1 W, and the results are also shown

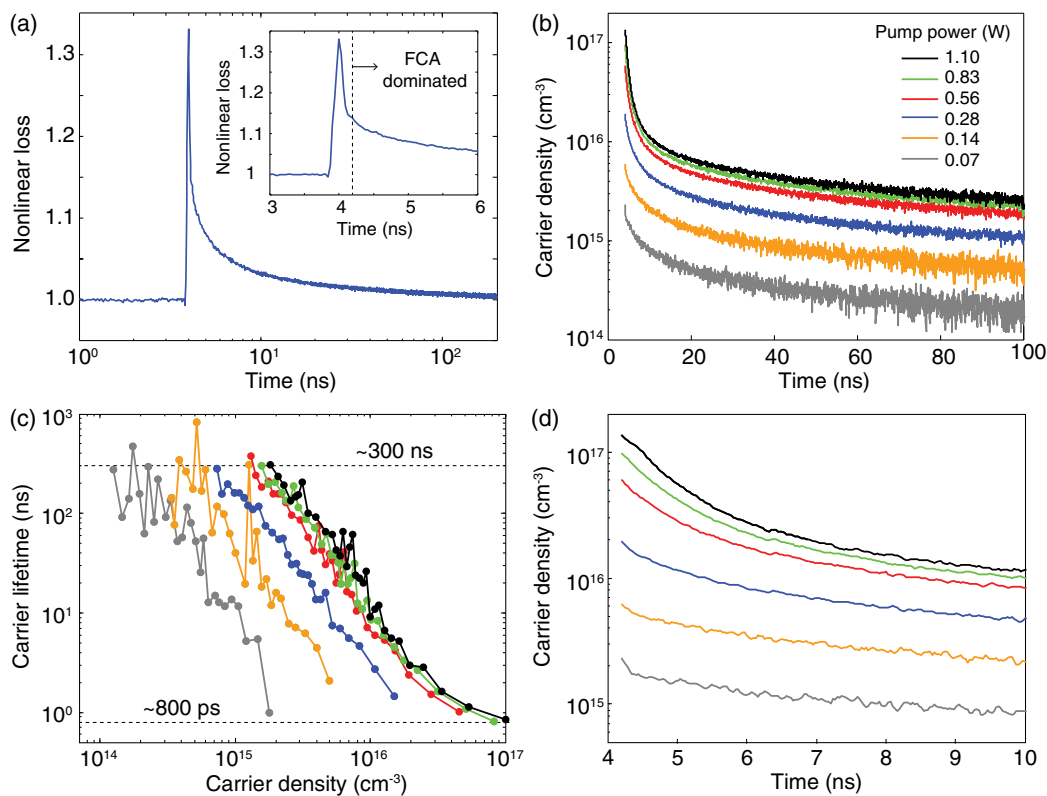


**Fig. 3.** Analysis of carrier density dynamics using 130 ps pump pulses. (a) Nonlinear loss as a function of time for 0.28 W pump power. The inset shows a zoom of the normalized nonlinear loss around the pump pulse in linear time scale. (b) Carrier density as a function of time for different pump peak powers. (c) Recombination lifetime as a function of carrier density for different pump peak powers. (d) Detail of the carrier density as a function of time for different pump peak powers in the first few nanoseconds.

in Fig. 3(b). A nonlinear decay behavior is observed in all curves, with faster decay rates at the beginning and slowing down as recombination progresses and the density falls. At the final stages of recombination, all curves approach the same slope; however, they differ significantly at early stages.

Several remarks can be made from this result. First, as already stated, the instantaneous carrier lifetime varies as the recombination evolves. This can be assessed quantitatively by numerically computing  $-\bar{N} \cdot (d\bar{N}/dt)^{-1}$  (see Supplement 1 for details in the numerical slope computation). The results are shown in Fig. 3(c) for the same power levels from Fig. 3(b). In all curves, the instantaneous lifetime varies from a slow limit of  $\sim 300$  ns to a fast limit of  $\sim 800$  ps. This represents more than 2 orders of magnitude reduction in the instantaneous lifetime as the density decays over almost 3 orders of magnitude. As already mentioned, the slow decay limit can be seen directly from Fig. 3(b) (here, it is important to ensure that the probe power is low enough not to impact the slow decay lifetime—see Supplement 1 for details). The fast limit can be appreciated in Fig. 3(d), which shows the density decay at the first few nanoseconds.

A second remarkable observation is that the lifetime is not simply a function of the carrier density. This is seen directly in Fig. 3(c), in which each curve has a different instantaneous lifetime for the same value of excess carrier density. The same conclusion can be drawn directly from the decay curves in Fig. 3(b), where at a given density value, the decay trajectory, that is,  $\bar{N}(t)$  is different for different initial values  $\bar{N}(0)$ , a form of memory in

the decay dynamics. In Section 4, we provide an explanation to this observation in terms of carrier trapping at the recombination centers, which leads to electrons and holes following different decay curves.

A final important observation in Fig. 3(c) is regarding the curves corresponding to the highest peak power levels. Note that the decay lifetime remains fast at around a few nanoseconds for a wide range of densities between  $10^{16}$  and  $10^{17}$   $\text{cm}^{-3}$ . In contrast, the lifetime for the lowest peak power curve increases from about 1 ns to over 100 ns in just one order of magnitude change in density, from  $10^{15}$  and  $10^{14}$   $\text{cm}^{-3}$ . This observation leads to the conclusion that operating at high carrier densities can be used as a strategy to obtain faster all-optical switching, as demonstrated at the end of the present section.

To summarize this discussion, three key observations are highlighted: (i) the carrier lifetime is faster initially and becomes slower as recombination evolves, with lifetimes ranging more than 2 orders of magnitude; (ii) the decay curve is not well defined by simply specifying the carrier density, but depends on its initial value; and (iii) operating at high density leads to faster decay rates for a wider density range. This behavior is discussed in detail in Section 4, considering the statistics of trap-assisted recombination process.

Once the carrier recombination dynamics have been analyzed, we now demonstrate how they are affected by the pump power level and the accumulated free carriers of previous pump pulses. We used long pump pulses (10 and 20 ns) to quantify not only

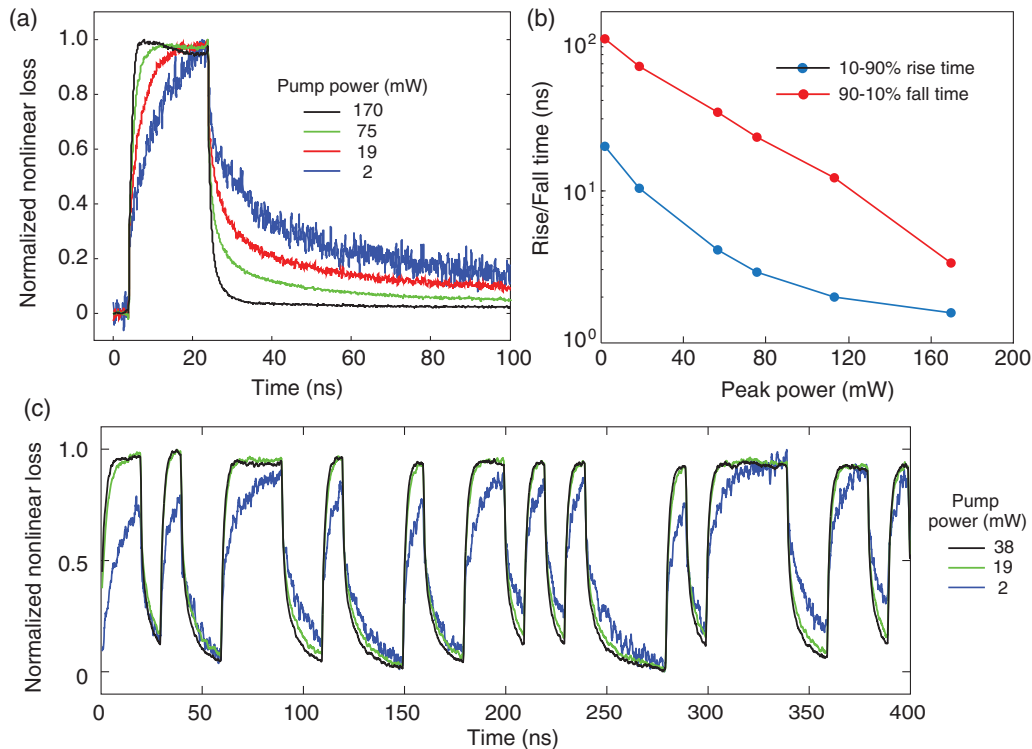


**Fig. 4.** Analysis of the carrier recombination dynamics using 20 ns pulses. (a) Normalized nonlinear loss for pump power levels of 2, 19, 75, and 170 mW. (b) Rise and fall times for different pump peak powers. (c) Nonlinear loss for a pseudo-random sequence of 10 ns pulses for three power levels of 2, 19, and 38 mW.

the decay rate but also the carrier build-up dynamics. Figure 4(a) shows the normalized nonlinear losses obtained for various pump power levels ranging from  $\sim 2$  to  $\sim 170$  mW. As expected from the previous dynamic analysis, higher pump power results in a faster response not only in the decay stage but also in the build-up stage. Figure 4(b) shows the rise and fall times calculated as the period it takes for the nonlinear loss to change from 10% to 90% and from 90% to 10%, respectively. The curves confirm a strong reduction in response time with increased pump power. Figure 4(c) shows the nonlinear loss measured for 10 ns pump pulses in a 40-symbol pseudo-random sequence at different power levels. This results confirms that higher pump power results in a faster behavior. It is interesting to note that since the instantaneous recombination rate strongly depends on the carrier dynamics, the dynamics are word-dependent. This can be appreciated at the beginning of the sequence: because the initial carrier density in the waveguide was low, the system is relatively slow, especially for 2 mW pump power. As free carriers are accumulated, the system becomes faster. This suggests a strategy to increase the overall speed by injecting a CW pump component to offset the excess carrier density, similar to what is explored in the context of solar cells [31].

We make a final comment in this section regarding the absolute values of the lifetimes reported here. The minimum lifetime at high carrier density is observed at around 800 ps. This is not, however, a fundamental limit. As we discuss in detail in the next section, this value can be reduced by either increasing the density of recombination centers (e.g., by increasing the surface trap density on the waveguide side and top walls), as well as reducing the waveguide dimensions, since in surface

recombination the lifetime is directly proportional to the waveguide size.

#### 4. DISCUSSION

There are two key observations in our experiments that the present discussion elucidates: first, the non-exponential decay curve has faster rates initially and slower rates at the final stage. Second, the fact that the shape of the decay curve depends on the initial condition, that is, on the initial excess carrier concentration, a form of memory behavior. These observations are qualitatively explained in terms of trap-assisted recombination. Although this is a well established process [22,24,31], its application in silicon photonic waveguides and cavities remains unexplored to the best of our knowledge. Auger recombination also plays a role in the high-density curves, and it should be included in a quantitative analysis.

Through trap-assisted recombination, an excess carrier, say an excess electron, is first captured in a trap state and eventually transferred to the valence band when an excess hole is captured by the same trap state. In TPA, excess electrons and holes are generated in equal numbers. However, it may occur that as recombination takes place, a significant unbalance is created between the density of excess electrons in the conduction band ( $n_e$ ) and the density of excess holes in the valence band ( $p_e$ ). This unbalance simply means that a significant fraction of electrons (or holes) remains in the traps for a certain period of time. In other words, electrons and holes do not necessarily decay at the same rate due to trapping. In our experiments, we measure absorption due to free carriers and cannot distinguish between

free electrons and free holes. In fact, the decay dynamic we observe experimentally reflects very nearly the dynamics of the sum of excess electron and hole concentrations. The exact FCA coefficient is given by the weighed sum of excess carriers  $(8.5n_e + 6.0p_e) \times 10^{-18} \text{ cm}^{-1}$ , each multiplied by its own absorption cross-section [5,6]. However, for simplicity, we discuss the behavior of the total excess density  $n_e + p_e$ . As we shall see, initially one type of carrier (electron or hole) decays faster than the other due to trapping, resulting in a non-exponential decay curve for the total  $n_e + p_e$ .

In order for significant trapping to occur, the density of traps ( $D_t$ ) must be relatively large—at least comparable to the density of excess carriers. If the trap density is too small, there cannot be a significant unbalance between  $n_e$  and  $p_e$ , because even if all traps are filled, the total number of trapped carriers would still be small compared to the total number of free carriers. In the absence of trapping, excess electrons decay at the same rate as excess holes. This regime is usually referred to as Shockley–Read–Hall (SRH) recombination [22,24]. Interestingly, it can also lead to non-exponential decay, since lifetime for high-excess density is different from the lifetime for low-excess density. However, as we discuss here, in the absence of trapping one cannot explain the dependence of the transient decay curve on the initial condition—clearly observed in our experiments. In the SRH model, all transient decay curves follow the same path, and a change in initial condition is simply a time shift of the decay curve. In other words, in the SRH model the lifetime is a well defined function of carrier density, which is not in agreement with our experiments. We therefore attribute our observation to the presence of trapping.

Traps can be located throughout the volume of the silicon core or at the interface between silicon and silicon dioxide. The latter is usually assumed to dominate in nano-waveguide (i.e., with large surface-to-volume ratio) [20]. Based on a simple geometrical argument, it is possible to show that if surface traps dominate, then the smaller the waveguide is, the more likely significant trapping is to occur. This can be seen as follows: if the recombination is dominated by volume traps, then the fraction of traps that are occupied (i.e., captured an electron or a hole for donor-like or acceptor-like traps, respectively) is simply  $(p_e - n_e)/D_t$ . This simply states that any unbalance in excess electrons and holes must be in the traps so that charge neutrality is maintained. If  $D_t$  is large, then one can have a significant unbalance  $(p_e - n_e)$ , obviously limited to when occupancy reaches 100% (saturation of traps). Note that  $p_e$ ,  $n_e$ , and  $D_t$  are all volume densities and, therefore, scale together as the waveguide dimensions change. For traps located on the surface, this same line of argument leads to a surface-to-volume ratio dependency. The quantity  $(p_e - n_e)A_cL$  represents the total number of carriers that must be in the traps to maintain charge neutrality (here  $A_c = WH$  is the core area and  $L$  is the waveguide length). If we call  $D_s$  the density of traps per unit area and  $A_s = 2HL$  the sidewall area (assuming most traps to be located on the sidewalls), then the fraction of traps that is now occupied by excess carriers is simply  $(p_e - n_e)W/(2D_s)$ . This expression states that the smaller the waveguide width  $W$ , the higher the unbalance can be, even if one did not increase the trap surface density  $D_s$ . In here perhaps lies the explanation of why this nonlinear decay dynamics becomes readily evident in our nano-waveguide samples. In the discussion that follows we use the symbol  $D_t$  to represent the trap density. If applied to bulk traps,  $D_t$  directly gives

**Table 1. Definition of Variables and Parameters Used in the Simulation of Carrier Decay Dynamics (Expressions for the Rest of Parameters are Given in Supplement 1)**

Symbol	Definition	Value
$p_0$	Equilibrium hole concentration	$1 \times 10^{15} \text{ cm}^{-3}$
$v_n$	Electrons thermal velocity	$1.7 \times 10^7 \text{ cm/s}$
$v_p$	Holes thermal velocity	$1.3 \times 10^7 \text{ cm/s}$
$\phi$	Fermi level	0.24 eV
$\phi_t$	Trap energy level	0.50 eV
$E_g$	Bandgap energy	1.12 eV
$D_t$	Trap density	$10^{14} - 10^{16} \text{ cm}^{-3}$
$N_c$	Effective state density of cond. band	$2.8 \times 10^{19} \text{ cm}^{-3}$
$N_v$	Effective state density of val. band	$1 \times 10^{19} \text{ cm}^{-3}$
$\sigma_n$	Electron cross section	$2.1 \times 10^{-15} \text{ cm}^2$
$\sigma_p$	Hole cross section	$2.6 \times 10^{-16} \text{ cm}^2$

the trap volume density. However, if one applies the theory below to surface recombination, then  $D_t = 2D_s/W$  should be used. In what follows, a large trap density  $D_t$  should always be interpreted as either a truly increased surface density  $D_s$  or simply a reduction in the waveguide width  $W$ .

The decay dynamics for a single trap energy level are governed by the following nonlinear equations that couple together electron and hole excess densities [22,24,32,33]:

$$\frac{dn_e}{dt} = G - \frac{1}{\tau_n} \left[ \frac{(n_0 + n_1 + n_e)(n_e - p_e)}{D_t} + \frac{n_e n_1}{n_0 + n_1} \right], \quad (2)$$

$$\frac{dp_e}{dt} = G - \frac{1}{\tau_p} \left[ \frac{(p_0 + p_1 + p_e)(p_e - n_e)}{D_t} + \frac{p_e p_1}{p_0 + p_1} \right], \quad (3)$$

where  $G$  is the carrier generation rate and  $\tau_n = 1/(D_t \sigma_n v_n)$  and  $\tau_p = 1/(D_t \sigma_p v_p)$  are the shortest capture time constants for electrons and holes, respectively, that is, when all traps are unoccupied (here  $\sigma_n$  and  $\sigma_p$  are the electron and hole capture cross sections, whereas  $v_n$  and  $v_p$  are the thermal velocities of electrons and holes). The equilibrium electron and hole densities are  $n_0$  and  $p_0$  and  $n_1 = n_0 \cdot \exp(\phi_t - \phi)$  and  $p_1 = p_0 \cdot \exp(\phi - \phi_t)$ , respectively, where  $\phi$  is the Fermi level and  $\phi_t$  is the trap energy level (see Table 1).

Equations (2) and (3) can be handled more conveniently in terms of normalized variables. The electron, hole, and trap densities are normalized by the majority carrier density  $p_0$  and become, respectively,  $x = n_e/p_0$ ,  $y = p_e/p_0$ , and  $D = D_t/p_0$ . The time is normalized by the fastest decay time, in our case,  $\tau_n$ ; therefore  $t' = t/\tau_n$ . With that, we can re-write Eqs. (2) and (3) as

$$\frac{dx}{dt'} = g - \left[ \frac{(x-y)[x + a(1+b)]}{D} + \frac{x}{1+b} \right], \quad (4)$$

$$\frac{dy}{dt'} = g - \left[ \frac{\gamma(y-x)(y+1+b)}{D} + \frac{\gamma by}{1+b} \right], \quad (5)$$

where  $g = G\tau_n/p_0$  is the normalized generation rate,  $a = n_1/p_0$ ,  $b = p_1/p_0$ , and  $\gamma = \tau_n/\tau_p$ . Explicit expressions are summarized in Supplement 1.

To illustrate the transient decay (i.e., after generation has ceased), we numerically solved Eqs. (4) and (5) assuming an impulse excitation, so that  $x(0) = y(0)$  (as in a short pulse TPA-generated carriers), thus  $n(0) = x(0) + y(0)$  is the normalized total carrier density at the beginning of the transient decay. We chose a donor-like trap with electron capture cross section  $\sigma_n$  larger than hole capture cross section  $\sigma_p$ , which is typical for

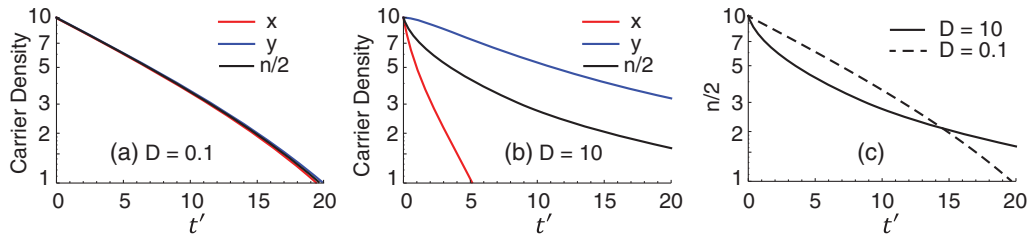


**Fig. 5.** Normalized carrier density transient decay for (a) small and (b) large trap density. (c) Total normalized carrier density  $n$  shown for both normalized trap densities  $D = 0.1$  and  $D = 10$ . In all figures, we plotted  $n/2$  for better visualization.

SiO<sub>2</sub>-Si interface [31], with  $\sigma_n = 8\sigma_p$ , resulting in  $\gamma = 0.1$  for the values of electron and hole thermal velocities given in Table 1. We also assumed that the trap energy level is located near the middle of the bandgap (at 0.5 eV above the valence band). Since our sample is an  $\sim 10 \Omega \text{ cm}$  p-type semiconductor, the initial trap occupancy is  $b/(1+b) = 4 \times 10^{-6}$ , which means that essentially all traps are unoccupied and ready to capture an electron. Other parameters used in the simulations are given in Table 1.

Figures 5(a) and 5(b) show the transient decay for small ( $D = 0.1$ ) and large ( $D = 10$ ) normalized trap densities, respectively. In red and blue are the decay for electrons ( $x$ ) and holes ( $y$ ), respectively, while in black we show the decay for the sum of electron and hole densities  $n(t') = x(t') + y(t')$  (divided by two for better visualization). Clearly, for small trap density, both excess electrons and excess holes decay at the same rate (i.e., no significant trapping occurs). On the other hand, for large trap density, electrons decay faster than holes. It is interesting to note that in this initial period most electrons are being trapped and not immediately returning to the valence band. Simultaneously, the excess holes initially find very few filled traps to be captured and, therefore, recombine slowly. As time passes, a significant fraction of the traps becomes filled and the electron capture rate decreases, while the hole capture rates increases. After long enough time (not shown here) the decay lifetime reaches a steady state, with equal values for both electrons and holes.

As a result of these dynamics, the decay curve for the total (normalized) density  $n$  also becomes very nonlinear. Initially, it decays following the fast electron decay. At longer times, the density of electrons becomes much smaller than that of holes, and then  $n$  decays following the slower hole transient decay. In Fig. 5(c), we show  $n/2$  for both small and large trap densities for comparison. It is quite clear that the initial decay is faster for

the large trap density, and the nonlinear behavior is more evident. At longer times, however, it may take even longer for the trapped electrons to recombine back to the valence band. This example illustrates that modeling carrier transients in small-scale silicon waveguides cannot be accurately performed with a single lifetime constant to explain our experimental observations.

The transient decay dependency on the initial carrier density observed in our experiment can be also qualitatively explained by this model. Figure 6(a) shows the transient decay for various initial carrier densities. All curves were obtained for the same set of parameters as before, assuming relatively large trap density ( $D = 10$ ), and varying only the initial excess carrier density. Very clearly, the initial decay is non-exponential and qualitatively agrees with the experimental results in Fig. 3(b). Moreover, none of the curves are a simple time shift of the other. Take, for example, the curves corresponding to initial density  $n = 100$  (in black) and  $n = 10$  (in green). At  $t' \approx 20$ , the black curve has reached  $n = 10$ , and the remaining decay curve is completely different from the curve corresponding to initial density  $n = 10$ . A simple way to evaluate this is to compute the instantaneous carrier lifetime and plot that as a function of the instantaneous carrier density [as performed for the experimental data in Fig. 3(c)]. The result is shown in Fig. 6(b), where we can see that different curves exhibit different lifetimes for the same instantaneous carrier density. Once again, a qualitative agreement with the experimental results in Fig. 3(c) is obtained. This memory-like effect on the total density occurs because the ratio between trap density and initial excess carriers determines how fast the electrons decay at the initial stages of recombination [34].

The dashed lines in Fig. 6(b) represent the limits (initial and final) for the normalized carrier lifetime. These limits can be calculated as  $\tau_0 = 2(1+b)$  and  $\tau_\infty = D(1+b)\gamma^{-1}[Db + (1+b)^2]^{-1}$ , respectively [22]. For traps near the middle of the bandgap,  $b$  is

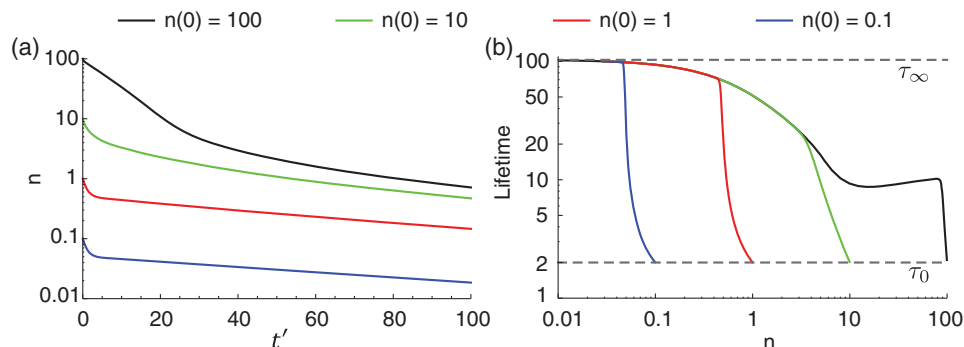


**Fig. 6.** (a) Transient decay and (b) instantaneous lifetime for different initial carrier densities. Each curve was calculated using the simulation parameters in Table 1 and large trap density ( $D = 10$ ).

approximately zero; therefore,  $\tau_0 = 2$  and  $\tau_\infty = D\gamma^{-1}$ . Using the definitions in Table 1, we can convert the normalized lifetimes to absolute values:  $t_0 = W/(v_n\sigma_n D_i)$  and  $t_\infty = 1/(v_p\sigma_p p_0)$ . Note that, while  $t_0$  can be reduced by simply decreasing the waveguide dimension  $W$ , the long lifetime limit  $t_\infty$  remains unchanged. From our measurements,  $t_\infty \approx 300$  ns and, using the parameters from Table 1, we can estimate the capture cross section for holes to be  $\sigma_p \approx 2.6 \times 10^{-16}$  cm<sup>2</sup>. This value is in agreement with measurements based on small pulse deep level transient spectroscopy [31]. However, the estimated cross section depends on the assumed thermal equilibrium hole density  $p_0$ , which we calculated based on the unprocessed silicon-on-insulator (SOI) resistivity. Precise characterization of the in-waveguide Fermi level [35] would be necessary for an accurate estimate of the cross section. Nevertheless, if the in-waveguide Fermi level is lower than that assumed here [35], no significant change in the dynamics is expected. This is because a lower Fermi level results in even lower trap occupancy, and therefore, the assumption  $b \approx 0$  still holds. If however, the Fermi level increases dramatically, say close to the trap level within one or two  $k_B T$ , or even above it, then the trap occupancy would change significantly and the initial electron decay rate would slow down [22,32,33]. From our measurements,  $t_0 = 0.8$  ns and, assuming again that  $\sigma_n = 8\sigma_p$ , we can estimate the order of magnitude of the surface trap density as  $D_i = W/(v_n\sigma_n t_0)$ . Using the parameters from Table 1, we obtain  $D_s \approx 1.6 \times 10^{12}$  cm<sup>-2</sup>, which is also in agreement with measurements on SiO<sub>2</sub>-Si interface [31,36].

The general behavior in the transient decay discussed in the present analysis is relatively robust to the choice of parameters ( $a$  and  $b$ ). One important point is regarding the parameter  $b$ , which is related to the thermal equilibrium trap occupancy: as long as the trap energy level is a few  $k_B T$  above the Fermi level, the occupancy level is near zero and  $b \approx 0$ . For a p-type semiconductor, in which the Fermi level is close to the valence band (in our case, we assumed 0.24 eV above the valence band that corresponds to the Fermi level of 10- $\Omega \cdot$  cm p-doped silicon), this practically means the trap energy levels can be anywhere near the mid-gap or on the top-part of the bandgap and  $b$  is still approximately zero. This is especially important considering that a continuum of trap energy states exists in a SiO<sub>2</sub>-Si interface [31].

The model presented here explains the physical origin of the key experimental observations, such as the non-exponential decay curve with faster rates initially and slower rates at the final stage and the fact that the shape of the transient decay curve depends on the initial condition, that is, on the initial excess carrier concentration, a form of memory behavior. A rigorous quantitative analysis of the transient decay should include a continuum of trap-energies. Other important parameters are the capture cross sections and trap densities, which depend on the particular oxide used in the cladding and processing conditions. Detailed characterization of these parameters would be required for a complete understanding of the decay dynamics. At high densities, the Auger effect should also be included. Finally, pump depletion along the waveguide length should also be included (Supplement 1 shows the effect of longitudinal averaging on the observed decay lifetime). Given these limitations, a quantitative comparison between the single-flaw model and experiments is beyond the scope of this work (a reasonable agreement is obtained in Supplement 1, including the effect of pump depletion).

A final comment is that the assumption  $n_e(0) = p_e(0)$  is valid for an impulse optical excitation. However, if we use long enough

pulses as excitation, then excess electron and hole densities at the beginning of the transient decay, that is, after the pulse, may already be different. This should be modeled using the complete set of Eqs. (4) and (5). In both cases, short and long pulses, the excitation term  $g$  will depend on the position along the waveguide, since the pump laser will be attenuated as it propagates. A natural question that arises is then how uniform the carrier density along the propagation length is. This analysis is discussed in Supplement 1.

## 5. CONCLUSIONS

In conclusion, we have experimentally characterized the recombination dynamics in strip silicon nano-waveguides and revealed a complex decay dynamics, with lifetime varying as recombination evolves in time. The results were interpreted in terms of trapping in mid-bandgap trap states. In particular, the analysis suggests an increase in excess charge trapping as the waveguide surface-to-volume ratio increases. Our results open opportunities to control the recombination dynamics by increasing the density of surface traps as well as exploring different cladding materials with different flaw energy levels and perhaps increased capture cross sections. The carrier recombination dynamics observed in our experiments may impact several nonlinear applications and, along with the theoretical discussion, provides the basis for a more in-depth treatment of free-carrier dynamics.

**Funding.** São Paulo Research Foundation (FAPESP) (2008/57857, 2012/50259-8, 2015/11779-4, 2013/20180-3, 2015/04113-0); Conselho Nacional de Desenvolvimento Científico e Tecnológico (CNPq) (574017/2008-9); Coordination for the Improvement of Higher Education Personnel (CAPES).

<sup>†</sup>These authors contributed equally to this work.

See Supplement 1 for supporting content.

## REFERENCES

1. J. Leuthold, C. Koos, and W. Freude, "Nonlinear silicon photonics," *Nat. Photonics* **4**, 535–544 (2010).
2. T. Liang and H. Tsang, "Role of free carriers from two-photon absorption in Raman amplification in silicon-on-insulator waveguides," *Appl. Phys. Lett.* **84**, 2745–2747 (2004).
3. L. Yin and G. P. Agrawal, "Impact of two-photon absorption on self-phase modulation in silicon waveguides," *Opt. Lett.* **32**, 2031–2033 (2007).
4. A. Blanco-Redondo, C. Husko, D. Eades, Y. Zhang, J. Li, T. Krauss, and B. Eggleton, "Observation of soliton compression in silicon photonic crystals," *Nat. Commun.* **5**, 3160 (2014).
5. R. Soref and B. Bennett, "Electrooptical effects in silicon," *IEEE J. Quantum Electron.* **23**, 123–129 (1987).
6. Q. Lin, O. J. Painter, and G. P. Agrawal, "Nonlinear optical phenomena in silicon waveguides: modeling and applications," *Opt. Express* **15**, 16604–16644 (2007).
7. T. Baba, S. Akiyama, M. Imai, N. Hirayama, H. Takahashi, Y. Noguchi, T. Horikawa, and T. Usuki, "50-Gb/s ring-resonator-based silicon modulator," *Opt. Express* **21**, 11869–11876 (2013).
8. H. Xu, X. Xiao, X. Li, Y. Hu, Z. Li, T. Chu, Y. Yu, and J. Yu, "High speed silicon Mach-Zehnder modulator based on interleaved PN junctions," *Opt. Express* **20**, 15093–15099 (2012).
9. S. Park, K. Yamada, T. Tsuchizawa, T. Watanabe, H. Shinjima, H. Nishi, R. Kou, and S. Ichi Itabashi, "Influence of carrier lifetime on performance of silicon p-i-n variable optical attenuators fabricated on sub-micrometer rib waveguides," *Opt. Express* **18**, 11282–11291 (2010).

10. A. D. Bristow, N. Rotenberg, and H. M. Van Driel, "Two-photon absorption and Kerr coefficients of silicon for 850–2200 nm," *Appl. Phys. Lett.* **90**, 191104 (2007).
11. V. R. Almeida, C. A. Barrios, R. R. Panepucci, and M. Lipson, "All-optical control of light on a silicon chip," *Nature* **431**, 1081–1084 (2004).
12. L. Yin, Q. Lin, and G. P. Agrawal, "Soliton fission and supercontinuum generation in silicon waveguides," *Opt. Lett.* **32**, 391–393 (2007).
13. F. Leo, S.-P. Gorza, S. Coen, B. Kuyken, and G. Roelkens, "Coherent supercontinuum generation in a silicon photonic wire in the telecommunication wavelength range," *Opt. Lett.* **40**, 123–126 (2015).
14. H. Shin, W. Qiu, R. Jarecki, J. A. Cox, R. H. Olsson III, A. Starbuck, Z. Wang, and P. T. Rakich, "Tailorable stimulated Brillouin scattering in nanoscale silicon waveguides," *Nat. Commun.* **4**, 1944 (2013).
15. T. J. Johnson, M. Borselli, and O. Painter, "Self-induced optical modulation of the transmission through a high-Q silicon microdisk resonator," *Opt. Express* **14**, 817–831 (2006).
16. W. H. Pernice, M. Li, and H. X. Tang, "Time-domain measurement of optical transport in silicon micro-ring resonators," *Opt. Express* **18**, 18438–18452 (2010).
17. T. Carmon, L. Yang, and K. J. Vahala, "Dynamical thermal behavior and thermal self-stability of microcavities," *Opt. Express* **12**, 4742–4750 (2004).
18. T. Tanabe, H. Taniyama, and M. Notomi, "Carrier diffusion and recombination in photonic crystal nanocavity optical switches," *J. Lightwave Technol.* **26**, 1396–1403 (2008).
19. K. Nozaki, T. Tanabe, A. Shinya, S. Matsuo, T. Sato, H. Taniyama, and M. Notomi, "Sub-femtojoule all-optical switching using a photonic-crystal nanocavity," *Nat. Photonics* **4**, 477–483 (2010).
20. D. Dimitropoulos, R. Jhaveri, R. Claps, J. Woo, and B. Jalali, "Lifetime of photogenerated carriers in silicon-on-insulator rib waveguides," *Appl. Phys. Lett.* **86**, 071115 (2005).
21. Y. Liu and H. K. Tsang, "Time dependent density of free carriers generated by two photon absorption in silicon waveguides," *Appl. Phys. Lett.* **90**, 211105 (2007).
22. J. S. Blakemore, *Semiconductor Statistics* (Courier Corporation, 2002).
23. S. M. Sze and K. K. Ng, *Physics of Semiconductor Devices* (Wiley, 2006).
24. W. Shockley and W. Read, Jr., "Statistics of the recombinations of holes and electrons," *Phys. Rev.* **87**, 835–842 (1952).
25. D. K. Schroder, "Carrier lifetimes in silicon," *IEEE Trans. Electron Devices* **44**, 160–170 (1997).
26. D. A. Fishman, C. M. Cirloganu, S. Webster, L. A. Padilha, M. Monroe, D. J. Hagan, and E. W. Van Stryland, "Sensitive mid-infrared detection in wide-bandgap semiconductors using extreme non-degenerate two-photon absorption," *Nat. Photonics* **5**, 561–565 (2011).
27. Y. Zhang, C. Husko, S. Lefrancois, I. H. Rey, T. F. Krauss, J. Schröder, and B. J. Eggleton, "Non-degenerate two-photon absorption in silicon waveguides: analytical and experimental study," *Opt. Express* **23**, 17101–17110 (2015).
28. J. Meitzner, F. G. Moore, B. M. Tillotson, S. D. Kevan, and G. L. Richmond, "Time-resolved measurement of free carrier absorption, diffusivity, and internal quantum efficiency in silicon," *Appl. Phys. Lett.* **103**, 092101 (2013).
29. A. Singh, "Influence of carrier transport on Raman amplification in silicon waveguides," *Opt. Express* **418**, 12569–12580 (2010).
30. H. K. Tsang, P. A. Snow, I. E. Day, I. H. White, R. V. Pentyl, R. S. Grant, Z. Su, G. T. Kennedy, and W. Sibbett, "All-optical modulation with ultrafast recovery at low pump energies in passive InGaAs/InGaAsP multi-quantum well waveguides," *Appl. Phys. Lett.* **62**, 1451–1453 (1993).
31. A. G. Aberle, S. Glunz, and W. Warta, "Impact of illumination level and oxide parameters on Shockley–Read–Hall recombination at the Si–SiO<sub>2</sub> interface," *J. Appl. Phys.* **71**, 4422–4431 (1992).
32. K. C. Nomura and J. S. Blakemore, "Decay of excess carriers in semiconductors," *Phys. Rev.* **112**, 1607–1615 (1958).
33. K. C. Nomura and J. S. Blakemore, "Decay of excess carriers in semiconductors. II," *Phys. Rev.* **121**, 734–740 (1961).
34. R. Ahrenkiel, B. Keyes, and D. Dunlavy, "Intensity-dependent minority-carrier lifetime in III-V semiconductors due to saturation of recombination centers," *J. Appl. Phys.* **70**, 225–231 (1991).
35. L. Alloatti, C. Koos, and J. Leuthold, "Optical loss by surface transfer doping in silicon waveguides," *Appl. Phys. Lett.* **107**, 031107 (2015).
36. P. J. Caplan, E. H. Poindexter, B. E. Deal, and R. R. Razouk, "ESR centers, interface states, and oxide fixed charge in thermally oxidized silicon wafers," *J. Appl. Phys.* **50**, 5847–5854 (1979).